

Deep temperature variability in Drake Passage

Yvonne L. Firing¹, Elaine L. McDonagh¹, Brian A. King¹, Damien G. Desbruyères¹

¹National Oceanography Centre, Southampton, UK

Key Points:

- 21 annual occupations of SR1b in Drake Passage show large interannual variability in deep temperature
- Cooling due to isopycnal migration adds to trend of cooling on isopycnals
- Deep temperature variability related to positions of ACC fronts through simple proxy

Corresponding author: Yvonne L. Firing, yvonne.firing@noc.ac.uk

This article has been accepted for publication and undergone full peer review but has not been through the copyediting, typesetting, pagination and proofreading process which may lead to differences between this version and the Version of Record. Please cite this article as doi: 10.1002/2016JC012452

© 2016 American Geophysical Union
Received: Oct 07, 2016; Revised: Dec 05, 2016; Accepted: Dec 07, 2016

Abstract

Observations made on 21 occupations between 1993 and 2016 of GO-SHIP line SR1b in eastern Drake Passage show an average temperature of 0.53°C deeper than 2000 dbar, with no significant trend, but substantial year-to-year variability (standard deviation 0.08°C). Using a neutral density framework to decompose the temperature variability into isopycnal displacement (heave) and isopycnal property change components shows that approximately 95% of the year-to-year variance in deep temperature is due to heave. Changes on isopycnals make a small contribution to year-to-year variability but contribute a significant trend of $-1.4 \pm 0.6 \text{ m}^{\circ}\text{C}$ per year, largest for density (γ_n) > 28.1 , south of the Polar Front (PF). The heave component is depth-coherent and results from either vertical or horizontal motions of neutral density surfaces, which trend upward and northward around the PF, downward for the densest levels in the southern section, and downward and southward in the Subantarctic Front and Southern Antarctic Circumpolar Current Front (SACCF). A proxy for the locations of the Antarctic Circumpolar Current (ACC) fronts is constructed from the repeat hydrographic data and has a strong relationship with deep ocean heat content, explaining 76% of deep temperature variance. The same frontal position proxy based on satellite altimeter-derived surface velocities explains 73% of deep temperature variance. The position of the PF plays the strongest role in this relationship between ACC fronts and deep temperature variability in Drake Passage, although much of the temperature variability in the southern half of the section can be explained by the position of the SACCF.

1 Introduction

The ocean is responsible for absorbing 93% of the global energy imbalance since the 1970s [IPCC, 2013]. The Argo profiling float program has enabled investigators to deduce, with increasing confidence, trends in ocean temperature in the top 2000 m contributing 0.4 to 0.6 W m^{-2} to the global energy budget [Roemmich *et al.*, 2015; Wijffels *et al.*, 2016], with 67% to 98% of this increase found in the Southern Ocean. Decadal repeat hydrographic sections have shown significant deep warming over most of the Southern Ocean, giving an average warming trend of $2.5 \text{ m}^{\circ}\text{C yr}^{-1}$ between 2000 m and 4000 m south of the Subantarctic Front (SAF) [Purkey and Johnson, 2010; Desbruyères *et al.*, 2016a]. These decadal changes are associated with changes in the volume and properties of deep water masses, with Antarctic Bottom Water (AABW) warming, freshening, and decreasing in volume globally [Purkey and Johnson, 2012, 2013]. While these signals

are significantly different from zero over most of the Southern Ocean, they are also spatially and temporally variable [Purkey and Johnson, 2012; Johnson *et al.*, 2014]. The Scotia Sea seems to be an exception to the pattern of significant deep warming, with Purkey and Johnson [2010] and Desbruyères *et al.* [2016a] finding near-zero trends below 2000 m in this area over the 1990s and 2000s, and Johnson *et al.* [2014] finding warming before 2005 and cooling after 2005. Here we examine the apparently anomalous behavior of deep water in the Scotia Sea using annual repeat hydrographic data from GO-SHIP line SR1b (Figure 1a) between 1993 and 2016.

Interannual variability in Antarctic Bottom Water (AABW) properties in the Scotia Sea has been linked to wind-driven variability in the Weddell Gyre by way of changes in the properties and volume of AABW-precursor water exported from the Weddell to the Scotia Sea [Jullion *et al.*, 2010]. The total trends in deep temperature along repeat sections in the Southern Ocean, however, are dominated by isopycnal heave rather than by changes in properties on isopycnals [Desbruyères *et al.*, 2016b; Gille, 2008]. In the Antarctic Circumpolar Current (ACC), where isopycnals slope steeply, heave of deep isopycnals may be associated with lateral motion driven by surface dynamic forcing, and may parallel surface meander and eddy variability [Gille, 2008; Meijers *et al.*, 2011; Swart and Fyfe, 2012]. The positions of the ACC fronts have been shown to have a regionally-varying response to atmospheric variability [Dong *et al.*, 2006; Sallée *et al.*, 2008], with southward shifts over the last decades in some parts of the Southern Ocean [Sokolov and Rintoul, 2009; Meijers *et al.*, 2011] producing 1.2 W m^{-2} of warming, partially compensated for by -0.6 W m^{-2} of diabatic cooling [Meijers *et al.*, 2011]. Although Drake Passage and the Scotia Sea are one of the most topographically constrained sections of the ACC, front position here nevertheless is highly variable at a variety of time scales [Cunningham *et al.*, 2003; Firing *et al.*, 2011; Lenn *et al.*, 2008], with the Polar Front (PF) having a clearly bimodal position on SR1b [Cunningham *et al.*, 2003]. We will investigate the role of both vertical isopycnal heave and lateral movements of the ACC fronts in the variability and trends in deep temperature in Drake Passage.

The hydrographic data collected annually since 1993 on section on SR1b (Section 2) allow us to separate interannual variability from secular trends in deep temperature, investigating the contributions of isopycnal displacements (heave) and changes on isopycnals (Section 3) and the relationship between heave and the positions of the ACC fronts (Section 4).

2 Data

Hydrographic data have been collected on GO-SHIP line SR1b (Figure 1a) in most austral summers (between mid-November and mid-March) from November 1993 to January 2016, producing 21 full synoptic sections to date (Table 1; these sections are distributed over 20 out of the 23 austral summers in the interval). Sections are composed of 28 to 32 stations between the 350 m isobath near Elephant Island and the 200 m isobath at Burdwood Bank, with spacing ranging from 35 to 40 km in mid-passage to 2 km over the continental slopes [King and Firing, 2015].

Salinity data from the conductivity temperature and depth (CTD) sensor from each cruise have been calibrated using bottle samples and salinity standards [King and Firing, 2015, 1], and corrected for batch-to-batch salinity standard offsets (ranging from -1.5×10^{-3} psu to $+0.7 \times 10^{-3}$ psu, Kawano *et al.* [2006] and H. Uchida, pers. comm.). No batch correction was applied to data from JR16. The batch correction has a negligible effect on velocity and related quantities. It does change the partitioning between the isopycnal and heave components (Section 3) of temperature change, however, on average increasing (decreasing) the variance in the heave component in the northern (southern) part of the passage by approximately 1%, and subtracting approximately 10% from the heave component of the trend, with the opposite effects on the isopycnal components.

Because the northern end of the SR1b track has changed over time, we interpolate the observations from each occupation onto a common line (Figure 1a) based on water depth. Temperature and salinity profiles are smoothed using a 30-dbar Hanning window and then linearly interpolated onto a 10-dbar by 0.02-degree latitude grid. Bottom triangles are filled by interpolating or extrapolating from neighboring profiles, matching to the data above at the deepest observed depth. The relationships presented here are not sensitive to how the bottom triangles are treated, as long as the same area is compared for each occupation.

We compute neutral density γ_n [Jackett and McDougall, 1997], absolute salinity S_A and conservative temperature Θ [IOC *et al.*, 2010] from the gridded temperature and salinity profiles. The southward and upward slope of Θ and γ_n characteristic of the ACC is present in their means (Figure 1b). In Section 3 we use $\gamma_n(p, y, t)$, where p is pressure, y is the along-section distance, and t is time, to regrid the Θ sections in (γ_n, y) or (p, γ_n) coordinates, in order to separate the deviations of $\Theta(p, y, t)$ from the mean Θ field (Fig-

ure 1b) into isopycnal and heave components. For plotting we transform the results back to spatial coordinates using the mean $\bar{\gamma}_n(p, y)$ (Figure 1b).

We calculate the baroclinic cross-section velocity u_{ref} relative to a reference level p_{ref} by integrating the geostrophic shear:

$$u_{ref}(p, y, t) = \frac{1}{f(y)} \int_{p_{ref}(y)}^p \frac{-\partial\delta(p', y, t)}{\partial y} dp', \quad (1)$$

where p is the pressure vertical coordinate, y is the along-section distance (positive in the northward direction), f is the Coriolis parameter, and δ , the specific volume anomaly, depends on Θ and S_A [IOC *et al.*, 2010]. Using the bottom $p(y)$ (Figure 1b) for p_{ref} gives u_{bot} , the baroclinic velocity referenced to zero at the bottom.

Sea level anomaly (SLA) maps (MSLA-H) generated by the Copernicus Marine and Environment Monitoring Service (CMEMS) using data from multiple satellite altimeters are combined with the CNES-CLS13 mean dynamic topography (MDT) to produce sea surface height fields. The fields have been mapped onto a $1/4^\circ$ grid using length scales of 125 km [Ducet *et al.*, 2000]. We average the fields weekly (noting that each occupation of SR1b spans approximately 5 days) and interpolate sea surface height η to the SR1b line (Figure 1a) to compute surface geostrophic velocity across the line:

$$u^{ssh}(0, y, t) = \frac{-g}{f(y)} \frac{\partial\eta(y, t)}{\partial y}, \quad (2)$$

where g is the acceleration due to gravity.

3 Deep temperature changes, isopycnal displacements, and isopycnal property changes

The time series of average conservative temperature deeper than 2000 dbar over the whole SR1b section (Figure 1c) shows considerable year-to-year variability, with a standard deviation of 0.08°C , and a non-significant trend of $-2.3 \text{ m}^\circ\text{C yr}^{-1} \pm 5.1 \text{ m}^\circ\text{C yr}^{-1}$. The uncertainty given for this and subsequent trend estimates is a 95% confidence interval (that is, twice the standard error of the trend fit coefficient) based on the residual time series variance, rather than on spatial variability, and on the independence of each measurement. The lack of significant autocorrelations of the residuals, as well as the fact that in general the quantities with larger/smaller time series variance also exhibit larger/smaller latitudinal variance, both reflect the prevalence of eddy and meander variability (Section 3.2).

3.1 Isopycnal property/heave decomposition

Using the method of *Bindoff and McDougall* [1994], *Desbruyères et al.* [2014], and *Desbruyères et al.* [2016b], we use the vertical profiles of Θ and γ_n to separate the change over time in Θ at each depth and latitude into two components:

$$\left. \frac{d\Theta}{dt} \right|_p (y,t) \approx \left. \frac{d\Theta}{dt} \right|_n (y,t) - \left. \frac{dp}{dt} \right|_n (y,t) \overline{\frac{\partial \Theta}{\partial p}} (y,t), \quad (3)$$

where $|_p$ indicates evaluation at constant pressure level p , $|_n$ indicates evaluation at constant neutral density γ_n , and $\overline{(\partial \Theta / \partial p)}$ is the vertical gradient of the mean Θ field (Figure 1b). The first term on the right hand side corresponds to the change in Θ on isopycnals at a given latitude. The second term on the right hand side is a linear approximation for the change in Θ due to vertical displacements of isopycnals, or heave. The two terms are often associated, respectively, with changes in water mass properties and with dynamical variability, although the heave term also reflects changes in water mass renewal rates (as discussed by, e.g., *Desbruyères et al.* [2016b]).

We perform this decomposition on time series composed of the deviations of each occupation from the record mean (Figure 1b). Equation 3 produces no value at a point (p', y', t') for which $\overline{\gamma_n}(p', y')$ is not within the range of the $\gamma_n(p, y', t')$ profile. We consider only grid points where Equation 3 produces values for at least 50% of occupations, and linearly interpolate component time series over gaps. The trends presented are not sensitive to this interpolation. The error in the decomposition, captured by the difference between original and reconstructed temperature time series and trends (e.g. Figure 2a) is relatively small between 1000 dbar and 3600 dbar.

The decomposition of temperature trends into isopycnal and heave components (Figure 2a, Table 2) attributes nearly all of the considerable year-to-year variability in deep temperature to heave. The two components make equal contributions to the trend in section-averaged temperature deeper than 2000 dbar (Table 2), but because of the high variability in the heave component, only the trend in isopycnal temperature, at $-1.4 \pm 0.6 \text{ m}^\circ\text{C yr}^{-1}$, is significantly different from zero. Most of the isopycnal signal comes from the southern part of the section (Figure 2b), where both trend ($-2.2 \pm 0.9 \text{ m}^\circ\text{C yr}^{-1}$) and variability (standard deviation of 0.02°C) are larger than in the northern part of the section ($-0.8 \pm 0.5 \text{ m}^\circ\text{C yr}^{-1}$ and 0.01°C).

Isopycnal temperature variability (Figure 3b) is higher in the southern part of the section than north of the PF, reflecting the transition from younger Antarctic Bottom Water (AABW) to older Circumpolar Deep Water (CDW). The heave-driven temperature variability below 1000 dbar (Figure 3c), meanwhile, is highest in the PF and SAF, with moderate values in the Polar Frontal Zone (PFZ) and Antarctic Zone (AZ). The result is that heave accounts for 95% of the variance in deep temperature north of 58°S, and 80% of the variance in the southern part of the section.

A trend of cooling on isopycnals is found over most of the area denser than $\gamma_n = 28.1$, with the strongest signal close to $\gamma_n = 28.25$, while positive isopycnal temperature trends are found in the warmest, lightest deep waters, mostly above 2000 dbar (Figure 4c). The spatial signal in the total temperature trend below 1000 dbar (Figure 4a) is dominated by the spatial variability in the heave term (Figure 4e). The large heave-driven cooling trend in the PF and PFZ sets the average heave-driven (Figure 4f) and total temperature (Figure 4b) trends over the northern part of the section, and is several times larger than the isopycnal temperature trends (Figure 4d). Alternating bands of heave-driven warming and cooling produce a smaller averaged signal in the southern part of the section (Figure 4f); here the heave-driven trend is more than compensated for by cooling on isopycnals (Figure 4d) except near the bottom, where heave-driven warming associated with nearly uniform downward migration of the densest isopycnal ($\gamma_n = 28.3$, Figure 4e) dominates.

3.2 Vertical and horizontal stratification and isopycnal displacements

Apart from this area near the bottom in the southern part of the section, and over the northern continental slope, the heave signal below 1000 dbar tends to be horizontally banded, suggesting a contribution from lateral isopycnal shifts instead of or in addition to vertical displacements. In the time series, these fluctuations may be associated with eddies or meanders. The trend in isopycnal position over time (Figure 4e), meanwhile, is consistent with northward migration of the strong density gradient associated with the PF over a range of depths (compare initial and final positions of the γ_n contour inflection point at the southern edge of the PF in Figure 4e).

In the presence of a large-scale monotonic horizontal density gradient such as that found in the ACC (that is, isopycnals sloping in one direction, as in Figure 1b), the de-

composition into changes due to spatial displacement of isopycnals vs changes in properties of isopycnals can also be done in the horizontal, by exchanging p and y in Equation 3. Additionally, where the same water mass properties are found across a range of latitudes, such that, at each time, the vertical profile T-S (temperature-salinity) curves and the T-S curves on pressure levels overlie each other, the partitioning between isopycnal change and isopycnal displacement components should be the same for the horizontal decomposition as for the vertical. Such a tight T-S relationship (Figure 5) is found on SR1b below 1000 dbar and north of 60°S (that is, north of the SACCF), signaling water that is well-mixed along isopycnals.

As a result, over most of the section, time series of temperature variability associated with horizontal isopycnal displacements closely follow those associated with vertical heave. Although temperature trends due to isopycnal displacements are small relative to the variability, the spatially-averaged horizontal displacement-driven and reconstructed total trends (not shown) in the southern and northern parts of the section echo their vertical counterparts (Figure 4f and Figure 4b). In most of the northern part of the section, the horizontal (not shown) and vertical (Figure 4e) isopycnal displacement-driven trends are nearly identical even without spatial averaging, reflecting the strong horizontal density gradients and relatively large scales of the eddy and meander variability. In the AZ, however, the relatively small background horizontal density gradient is overwhelmed by the noise of the smaller-scale eddies in the horizontal displacement term, with the result that the spatial pattern of temperature trends in the southern part of the section is not well captured by the horizontal decomposition.

4 Deep temperature variability and frontal position

The positions of the ACC fronts exhibit wind-driven and internal meander and eddy variability on a variety of time scales [Sokolov and Rintoul, 2009; Lenn *et al.*, 2008], and have previously been related to temperature trends in the upper Southern Ocean [Morrow *et al.*, 2008; Sokolov and Rintoul, 2003; Gille, 2008; Hutchinson *et al.*, 2016]. The dominance of the isopycnal displacement (heave) contribution to deep temperature variance, discussed in the previous section, suggests that frontal position variability may also be a driver of deep temperature variability.

4.1 A frontal position proxy based on surface velocity

We compute a proxy for the positions and strengths of the ACC fronts (dynamically defined, as density gradient maxima):

$$D(t) = \int_{y_S}^{y_N} (f_0 - f(y)) u_{ref}(0, y, t) dy, \quad (4)$$

where y_S and y_N are the southern and northern limits of integration, f_0 is the section mean of f and $u_{ref}(0, y, t)$ is the baroclinic velocity at the sea surface relative to p_{ref} (Equation 1). Here we use u_{bot} , the baroclinic velocity relative to zero at the bottom, but the time dependence of D is not sensitive to the choice of reference level, as long as $p_{ref} \geq 1000$ dbar. We also compute D^{ssh} using satellite altimeter-derived surface total geostrophic velocity u^{ssh} (Equation 2) in place of baroclinic u_{ref} . D , which is qualitatively similar to the transport-weighted latitude index discussed by *Gille* [2014], depends on both the section-mean baroclinic velocity and the correlation between baroclinic velocity and latitude; it is more negative when transport is concentrated further north.

Integrating Equation 4 (with $u_{ref} = u_{bot}$) from the southern to the northern end of the section produces a D_0 which principally reflects variability in the positions of the fronts: it is barely correlated with the total baroclinic transport ($r = -0.18$, not shown), but has a correlation of $r = -0.76$ with baroclinic transport north of 57.5°S , a time series (not shown) which strongly reflects the bimodal PF position described by [*Cunningham et al.*, 2003]. We therefore will refer to D_0 as the integrated frontal position proxy.

Because the integrated frontal position proxy D_0 is dominated by the northern half of the passage, while temperature trends and variability are different in the southern and northern parts of the section (Section 3), we also consider D integrated over two latitude sub-ranges: a southern frontal position proxy, D_s , from 60.75°S to 59.23°S , and a northern frontal position proxy, D_n , from 57.41°S to 54.95°S . These latitude ranges were chosen to capture most of the temperature variance in the southern (south of 58°S) and northern (north of 58°S) portions of the passage, respectively, but the southern range of integration also roughly corresponds with the range of positions of the SACCF, and the northern range with the northern position of the PF through the PFZ and the SAF. D_n is thus very similar to D_0 , as it covers the latitude range with the largest velocity variance, and like D_0 is strongly sensitive to the position of the bimodal PF. The northern and southern frontal position indices D_n and D_s are correlated with transport in their latitude ranges with coef-

ficients of $r = -0.76$ and $r = 0.81$, respectively (the coefficient for D_s is positive because f in this latitude range is more negative than f_0).

4.2 Correlations with deep temperature

The integrated frontal position proxy D_0 explains 76% of the variance in section-averaged temperature ($\langle \Theta \rangle$) deeper than 2000 dbar (Figure 6a, dark blue), with more negative D_0 associated with lower temperature, as expected. Positive correlations between D_0 and Θ (Figure 6b) are concentrated north of 58°S, especially between 57.5°S and 56°S, in the PFZ. Correlations with $\langle \Theta(p) \rangle$ (Figure 6e) range from $r = 0.84$ at 1500 dbar to $r = 0.91$ at 3300 dbar, while correlations with the heave component (not shown) are approximately $r = 0.87$ in this depth range; correlations with D_0 decrease above and below these depths.

At each depth below 1000 dbar, the southern frontal position proxy D_s is positively correlated with temperature as far north as 57.5°S, although the highest values are found between 59.75°S and 58°S (Figure 6c). The northern frontal position proxy, D_n , which as noted above is very similar to D_0 , produces slightly higher correlations in the northern part of the section (Figure 6d). Correlations with D_s and D_n explain more than 50% of the variance in $\langle \Theta \rangle_S$ (Θ south of 58°S) and $\langle \Theta \rangle_N$ (Θ north of 58°S), respectively, at each depth between 1000 dbar and 3600 dbar (Figure 6e). They are higher for the northern pair, reaching $r = 0.93$ between 1500 dbar and 3000 dbar, compared to $r = 0.86$ in the same depth range in the southern half (Figure 6e). Correlations (not shown) between D and the heave-driven temperature time series are similar on average to those between D and total Θ , with D_s and D_n accounting for 60 to 75% and 80 to 88% of the southern and northern heave-driven temperature variability, respectively.

The above-mentioned decrease in correlation below 3300 dbar principally derives from the northern part of the section, where mid-passage topography means that the deeper levels are found only in the SAF latitude range, and thus temperature at these depths is not strongly affected by the position of the PF. The more gradual decrease with depth in $D_s, \langle \Theta \rangle_S$ correlation (Figure 6e), despite continued moderate positive correlations between D_s and $\Theta(p, y)$, echoes the decrease in temperature variance with depth in the southern part of the section (Figure 3a).

Not only are both the amplitudes and typical horizontal scales of lateral temperature and density gradients smaller in the southern part of the section, but density is less sensitive to temperature variability in colder waters; thus we expect the connection between D and either total or heave-driven temperature variability to be more obscured by noise in the southern portion of the section than in the north. For total temperature, the isopycnal property change component, relatively larger in the southern part of the section, is another source of noise in the D - Θ comparison.

In the northern part of the section, the lateral displacements of density gradients and those of pressure gradients appear to track each other closely, with the result that D_0^{ssh} and D_0 , and D_n^{ssh} and D_n , are well-matched (Figure 7a), and correlations of temperature time series with D^{ssh} have coefficients only 0.02 to 0.03 lower than those with baroclinic velocity-based D . The agreement between D_s and D_s^{ssh} is not as good, and the latter explains only 40% of deep temperature variability in the southern portion of the section. The orbital inclinations of the shorter-repeat-period satellites mean that the inherent resolution of the altimeter data at weekly time scales is lower toward the southern part of the section; thus we are not confident that the disagreement between D_s and D_s^{ssh} shows a looser relationship between density and pressure gradients in this region.

Scaling D_0 , D_s , and D_n to best fit the annual time series of $\langle \Theta(p > 2000) \rangle$, $\langle \Theta(p > 2000) \rangle_S$, and $\langle \Theta(p > 2000) \rangle_N$, respectively (Figure 7a) results in trends of the same sign as those in temperature (Table 2). The scaled D trends are larger than the temperature trends in each region, producing a positive residual trend in the north and averaged over the section, and a negative residual trend in the south, although the differences are within the uncertainty intervals. The Θ - (scaled) D residuals (Figure 7b) should include both isopycnal property variability and the component of heave-driven temperature variability not correlated with lateral displacements of isopycnal gradients (for example, the vertical and lateral migration of isopycnals induced by a uniform temperature change, or the heave associated with pure up/downwelling over some latitude range). The former contribution is not distinguishable from the noise: residual time series for each region (south, north, and whole section) are not correlated with isopycnal temperature variability in the corresponding region. They are moderately correlated with the heave-driven temperature time series, with coefficients ($r = 0.45$ to $r = 0.53$) implying that 0.02°C of the 0.08°C standard deviation (Table 2) of section-averaged total temperature deeper than 2000 dbar is associ-

ated with non-frontal-movement heave (or 0.01°C of 0.06°C in the southern portion of the section, and 0.02°C of 0.12°C in the northern part).

5 Discussion and Conclusions

Annual observations of temperature on SR1b in Drake Passage show an average temperature below 2000 dbar of 0.53°C and a trend of $-2.3 \pm 5.1 \text{ m}^{\circ}\text{C yr}^{-1}$ over the past 22 years. The 0.08°C standard deviation of the time series, responsible for the relatively large uncertainty on the trend, is more than enough to account for the change in trends ($-2 \text{ m}^{\circ}\text{C yr}^{-1}$ to $+8 \text{ m}^{\circ}\text{C yr}^{-1}$) from two pairs of surveys in the region reported by *Johnson et al.* [2014], and is consistent with the spatial-averaging based uncertainty estimates of *Purkey and Johnson* [2010] and others. In fact, to achieve a 95% confidence interval smaller than $\pm 2.3 \text{ m}^{\circ}\text{C yr}^{-1}$ would require 15 more annual occupations of SR1b added to the current record.

The negative trend in SR1b deep temperature results from the combination of smaller negative trends in both temperature on isopycnals and the component of *in situ* temperature change due to isopycnal displacements [heave, as also found by *Desbruyères et al.*, 2016b]. The former component has much smaller variability from occupation to occupation, and thus its trend is distinguishable above the noise, with deep isopycnal temperature changes contributing a significant cooling trend of $-1.4 \pm 0.6 \text{ m}^{\circ}\text{C yr}^{-1}$ to temperature deeper than 2000 dbar averaged over the section, and a corresponding freshening of $-2.7 \pm 1.0 \times 10^{-4} \text{ psu yr}^{-1}$. Deep isopycnal temperature trends broadly follow water mass boundaries, with isopycnal warming for upper CDW (UCDW), found as deep as 2500 dbar at the northern end of the section, and isopycnal cooling nearly everywhere else. The negative isopycnal temperature trend in waters denser than $\gamma_n = 28.1$, with maximum amplitude around $\gamma_n = 28.25$, is consistent with the freshening of AABW reported by *Jullion et al.* [2013].

The heave-driven warming of AABW around $\gamma_n = 28.3$ counteracts the isopycnal cooling there, producing a net warming trend in the bottom few hundred meters in the southern part of the section. The associated isopycnal position trends imply an expansion of denser AABW with $\gamma_n \sim 28.3$. Other analyses [*Purkey and Johnson*, 2012] have indicated that this expansion is localised to Drake Passage/the western Scotia Sea, with contraction found at the eastern edge of the Scotia Sea [section A16 *Purkey and Johnson*,

2012] as well as in most of the rest of the Southern Ocean. As with the total temperature trend discussed above, large occupation-to-occupation variability in isopycnal positions means that none of these isopycnal position or heave-driven temperature trends are significant (that is, larger than their 95% confidence intervals) with the current record length.

Over most of the section (north of 60°S and deeper than ~1500 dbar), the same isopycnal temperature trends can be derived by considering either vertical or horizontal (pressure level) profiles, reflecting the fact that water is extremely well-mixed along isopycnals on SR1b (below the surface layer). This uniformity appears to characterise not only CDW, which has had considerable time in its journey around the ACC to be homogenized by eddy stirring, but also most of the AABW on the section. The consistency of properties and trends on isopycnals here contrasts with the differing adiabatic trends in intermediate waters south of Africa reported by *Hutchinson et al.* [2016].

This along-isopycnal uniformity does not preclude time variability in isopycnal properties. Isopycnal temperature variance in the very lightest of the waters deeper than 1000 dbar, in both the southern and northern parts of the section, may partially derive from the same seasonal variability in properties of CDW in the top 1000 m described by *Evans et al.* [2014]; however, this variance does not appear to extend to the deeper, more isolated LCDW in the northern part of the section. In the southern part of the section, changes on isopycnals contribute up to 20% of the *in situ* temperature variance in the AABW layers. Variability in AABW properties in Drake Passage, on time scales from monthly [*Rubython et al.*, 2001] to interannual [*Jullion et al.*, 2010], has been related to wind-driven changes in Weddell Sea Deep Water (WSDW) entering the region. Such variability in WSDW export may be reflected not only in properties but also in volume of AABW or its sub-classes, and thus may appear in the heave-driven as well as the isopycnal component of temperature variance. Heave-driven and isopycnal temperature time series are not correlated in the AABW layer in general, but are significantly correlated (coefficients of $r = 0.5$ to $r = 0.8$) around the boundary between AABW and LCDW. They are also significantly negatively correlated around the boundary between LCDW and UCDW in the northern part of the section.

Heave-driven temperature change due to modulation of the overturning circulation would be expected to mirror its spatial structure. For the most part (aside from the area near the bottom in the southern part of the section, and the area immediately adja-

cent to the northern continental slope), however, the heave-driven temperature trends and variability on SR1b are dominated by multiple horizontal bands of alternating sign, suggesting they might just as well be produced by depth-coherent lateral movements of the sloping isopycnals. *Meijers et al.* [2011] previously found Southern Ocean temperature trends to be dominated by such adiabatic, dynamically-driven shifting of the ACC fronts.

We have constructed a proxy for the positions of the fronts on SR1b based on the correlation between surface baroclinic velocity and latitude, and find that correlations with this proxy, D , explain 76% of the section-averaged deep temperature variance. Due to the strength and bimodal nature of the PF [*Cunningham et al.*, 2003], the section-wide proxy is strongly influenced by the PF position; a similar proxy (D_n) capturing only the PF and SAF positions explains 86% of the variance in deep temperature north of 58°S (that is, in and north of the PF), while one covering the SACCF position (D_s) explains 74% of the variance in deep temperature south of 58°S (Figure 7c). Although *Cunningham et al.* [2003] previously noted an association between the northward position of the PF and cold AABW temperatures, and vice versa, in the Ona Basin (that is, on the southern part of SR1b), the latitude of the SACCF appears to be an even stronger predictor of deep temperature in this region.

In the northern part of the section, deep temperature variability is predicted nearly as well ($> 70\%$ variance explained) by using satellite altimeter-derived surface geostrophic velocity (rather than baroclinic velocity) to construct a version of the frontal position proxy (D^{ssh}). This correspondence reflects the alignment between density and pressure gradients, or between deep and surface velocity maxima, in the ACC [*Watts et al.*, 2001; *Sun and Watts*, 2001; *Meijers et al.*, 2011; *Hutchinson et al.*, 2016]. Lower correlations in the southern part of the section may be due to the much smaller signal:noise ratio there. The weekly time series of scaled D^{ssh} (Figure 7a) contain substantial energy on a range of time scales from monthly to interannual, and imply that much of the variability in the annual repeat hydrographic sections is aliased sub-annual eddy variance. Additional sub-annual variance, such as the seasonal cycle in CDW thickness described by *Evans et al.* [2014], may appear only in vertical heave and thus not be captured by the frontal position proxy.

The difference between the deep temperature trend due to isopycnal heave and the deep temperature trend predicted by frontal position proxy D is small compared to the (considerable) uncertainty on either quantity. Speculating nevertheless, we note that the

more negative trend in D_n than in either total or heave-associated deep temperature would imply that the PF and SAF velocity maxima have moved farther north than the isopycnals in this region have, and that a generalized warming would produce just such a poleward trend in isopycnal positions relative to front position [e.g. *Gille, 2014*].

Our results reinforce the findings of *Desbruyères et al. [2016b]* of the importance of heave for deep temperature changes in the Southern Ocean and indeed globally, and confirm the suggestion of *Gille [2008]* and *Meijers et al. [2011]* that ACC temperature trends and variance are strongly influenced by movements of the ACC fronts, and that these movements can be identified in surface velocity or dynamic height. While the location of SR1b in the highly topographically constrained Drake Passage/Scotia Sea region may not be typical of the ACC as a whole, the connection between upper-ocean frontal movements and deep temperature, and their correlation via a simple proxy, relies on more widespread characteristics of the ACC, in particular its depth persistence and strong eddy variability. Previous estimates of deep Southern Ocean trends and their uncertainties [e.g. *Purkey and Johnson, 2010; Desbruyères et al., 2016a*] have attempted to account for possible aliasing of eddy and meander variability, and the results presented here highlight the importance of this consideration. They also suggest additional exploration of using frequent satellite surface observations to reduce aliasing of higher frequency signals [in the manner of *Lenn et al., 2008*] by infrequent full-depth hydrographic surveys.

Acknowledgments

We are grateful to G. Johnson, P. Abrahamsen, A. Meijers, and M. Meredith for helpful discussions. Thanks to H. Uchida for providing updated salinity standard batch corrections. This work was funded by the UK Natural Environment Research Council (NERC) under a National Capability award to the National Oceanography Centre (NOC) and through the Long Term Science-Multicentre (LTS-M) Ocean Regulation of Climate by Heat and Carbon Sequestration and Transports (ORCHESTRA) programme. The data used in this work are listed in the text and references. SR1b hydrographic data collection was funded by NERC and forms part of GO-SHIP (www.go-ship.org); the data are available from the British Oceanographic Data Centre (bodc.ac.uk). The Ssalto/Duacs altimeter products were produced and distributed by the Copernicus Marine and Environment Monitoring Service (CMEMS) (<http://www.marine.copernicus.edu>). MDT_CNES-CLS13 was produced by CLS (Collect Localisation Satellites) Space Oceanography Division and dis-

tributed by AVISO (Archiving, Validation, and Interpretation of Satellite Oceanographic data), with support from CNES (Centre National d'Etudes Spatiales) (<http://www.aviso.altimetry.fr>).

On behalf of all authors, the corresponding author states that there is no conflict of interest.

References

- Arndt, J. E., H. W. Schenke, M. Jakobsson, F. O. Nitsche, G. Buys, B. Goleby, M. Rebecco, F. Bohoyo, J. Hong, J. Black, R. Greku, G. Udintsev, F. Barrios, W. Reynoso-Peralta, M. Taisei, and R. Wigley (2013), The International Bathymetric Chart of the Southern Ocean (IBCSO) version 1.0—A new bathymetric compilation covering circum-Antarctic waters, *Geophysical Research Letters*, *40*(12), 3111–3117, doi:10.1002/grl.50413.
- Bindoff, N. L., and T. J. McDougall (1994), Diagnosing climate change and ocean ventilation using hydrographic data, *J. Phys. Oceanogr.*, *24*, 1137–1152.
- Cunningham, S. A., S. G. Alderson, B. A. King, and M. A. Brandon (2003), Transport and variability of the Antarctic Circumpolar Current in Drake Passage, *J. Geophys. Res.*, *108*(C5), 8084, doi:10.1029/2001JC001147.
- Desbruyères, D. G., E. L. McDonagh, B. A. King, F. K. Garry, A. T. Blaker, B. I. Moat, and H. Mercier (2014), Full-depth temperature trends in the northeastern Atlantic through the early 21st century, *Geophys. Res. Lett.*, *41*, 7971–7979, doi:10.1002/2014gl061844.
- Desbruyères, D. G., S. G. Purkey, E. L. McDonagh, G. C. Johnson, and B. A. King (2016a), Deep and abyssal ocean warming from 35 years of repeat hydrography, *Geophys. Res. Lett.*, *43*, 10,356–10,365, doi:10.1002/2016gl070413.
- Desbruyères, D. G., E. L. McDonagh, B. A. King, and V. Thierry (2016b), Global and full-depth ocean temperature changes during the early 21st century from Argo and repeat hydrography, *Submitted to J. Clim.*
- Dong, S., J. Sprintall, and S. T. Gille (2006), Location of the Antarctic Polar Front from AMSR-E satellite sea surface temperature measurements, *J. Phys. Oceanogr.*, *36*, 2075–2089.
- Ducet, N., P. Y. Le Traon, and G. Reverdin (2000), Global high-resolution mapping of ocean circulation from TOPEX/Poseidon and ERS-1 and -2, *J. Geophys. Res.*, *40*(C8), 19,477–19,498.

- Evans, D. G., J. D. Zika, A. C. N. Garabato, and A. J. G. Nurser (2014), The imprint of Southern Ocean overturning on seasonal water mass variability in Drake Passage, *J. Geophys. Res.*, *119*, 7987–8010, doi:10.1002/2014jc010097.
- Firing, Y. L., T. K. Chereskin, and M. R. Mazloff (2011), Vertical structure and transport of the Antarctic Circumpolar Current in Drake Passage from direct velocity observations, *J. Geophys. Res.*, *116*(C08015), doi:10.1029/2011JC006999.
- Gille, S. T. (2008), Decadal-scale temperature trends in the southern hemisphere ocean, *J. Clim.*, *21*, 4749–4765, doi:10.1175/2008jcli2131.1.
- Gille, S. T. (2014), Meridional displacement of the Antarctic Circumpolar Current, *Phil. Trans. R. Soc. A*, *372*(20130273), doi:10.1098/rsta.2013.0273.
- Hutchinson, K., S. Swart, A. Meijers, I. Ansorge, and S. Speich (2016), Decadal-scale thermohaline variability in the Atlantic sector of the Southern Ocean, *J. Geophys. Res.*, *121*, 3171–3189, doi:10.1002/2015jc011491.
- IOC, SCOR, and IAPSO (2010), *The international thermodynamic equation of seawater – 2010: Calculation and use of thermodynamic properties*, Intergovernmental Oceanographic Commission.
- IPCC, I. P. o. C. C. (2013), *Intergovernmental Panel on Climate Change (IPCC), Climate Change 2013: The Physical Science Basis*, Cambridge Univ. Press, Cambridge, UK.
- Jackett, D. R., and T. J. McDougall (1997), A neutral density variable for the world's oceans, *J. Phys. Oceanogr.*, *27*, 237–253.
- Johnson, G. C., K. E. McTaggart, and R. Wanninkhof (2014), Antarctic Bottom Water temperature changes in the western South Atlantic from 1989 to 2014, *J. Geophys. Res.*, *119*, doi:10.1002/2014jc010367.
- Jullion, L., S. C. Jones, A. C. Naveira Garabato, and M. P. Meredith (2010), Wind-controlled export of Antarctic Bottom Water from the Weddell Sea, *Geophys. Res. Lett.*, *37*(L09609), doi:10.1029/2010gl042822.
- Jullion, L., A. C. Naveira Garabato, M. P. Meredith, P. R. Holland, P. Courtois, and B. A. King (2013), Decadal freshening of the Antarctic Bottom Water exported from the Weddell Sea, *J. Clim.*, *26*, 8111–8125, doi:10.1176/jcli-d-12-00765.1.
- Kawano, T., M. Aoyama, T. Joyce, H. Uchida, Y. Takatsuki, and M. Fukasawa (2006), The latest batch-to-batch difference table of standard seawater and its application to the WOCE onetime sections, *J. Oceanogr.*, *62*, 777–792.

- King, B. A., and Y. Firing (2015), RRS james clark ross cruise JR306: Hydrographic measurements on WOCE line SR1b, *Tech. Rep. 31*, National Oceanography Centre.
- Lenn, Y.-D., T. K. Chereskin, and J. Sprintall (2008), Improving estimates of the Antarctic Circumpolar Current streamlines in Drake Passage, *J. Phys. Oceanogr.*, *38*, 1000–1010.
- Meijers, A. J. S., N. L. Bindoff, and S. R. Rintoul (2011), Frontal movements and property fluxes: contributions to heat and freshwater trends in the Southern Ocean, *J. Geophys. Res.*, *116*(C08024), doi:10.1029/2010jc006832.
- Morrow, R., G. Valladeau, and J.-B. Sallee (2008), Observed subsurface signature of Southern Ocean sea level rise, *Prog. Oceanogr.*, *77*, 351–366, doi:10.1016/j.pocean.2007.03.002.
- Orsi, A. H., T. Whitworth, III, and W. D. Nowlin, Jr (1995), On the meridional extent and fronts of the Antarctic Circumpolar Current, *Deep Sea Res. I*, *42*(5), 641–673.
- Purkey, S. G., and G. C. Johnson (2010), Warming of global abyssal and deep Southern Ocean waters between the 1990s and 2000s: contributions to global heat and sea level rise budgets, *J. Clim.*, *23*, 6336–6351, doi:10.1175/2010jcli3682.1.
- Purkey, S. G., and G. C. Johnson (2012), Global contraction of Antarctic Bottom Water between the 1980s and 2000s, *J. Clim.*, *25*, 5830–5844, doi:10.1175/jcli-d-11-00612.1.
- Purkey, S. G., and G. C. Johnson (2013), Antarctic Bottom Water warming and freshening: contributions to sea level rise, ocean freshwater budgets, and global heat gain, *J. Clim.*, *25*, 6105–6122, doi:10.1175/jcli-d-12-00834.1.
- Roemmich, D., J. Church, J. Gilson, D. Monselesan, P. Sutton, and S. Wijffels (2015), Unabated planetary warming and its ocean structure since 2006, *Nat. Clim. Change*, *5*, 240–245, doi:10.1038/nclimate2513.
- Rubython, K. E., K. J. Heywood, and J. M. Vassie (2001), Interannual variability of bottom temperatures in Drake Passage, *J. Geophys. Res.*, *106*(C2), 2779–2793, doi:10.1029/2000JC900114.
- Sallée, J. B., K. Speer, and R. Morrow (2008), Response of the Antarctic Circumpolar Current to atmospheric variability, *J. Clim.*, *21*, 3020–3039, doi:10.1175/2007jcli1702.1.
- Smith, W. H. F., and D. T. Sandwell (1997), Global seafloor topography from satellite altimetry and ship depth soundings, *Science*, *277*, 1957–1962.
- Sokolov, S., and S. Rintoul (2003), Subsurface structure of interannual temperature anomalies in the Australian sector of the Southern Ocean, *J. Geophys. Res.*, *108*(C9), 3285, doi:10.1029/2002JC001494.

Sokolov, S., and S. R. Rintoul (2009), Circumpolar structure and distribution of the Antarctic Circumpolar Current fronts: 2. variability and relationship to sea surface height, *J. Geophys. Res.*, *114*(C11019), doi:10.1029/2008JC005248.

Sun, C., and D. R. Watts (2001), A circumpolar gravest empirical mode for the Southern Ocean hydrography, *J. Geophys. Res.*, *106*(C2), 2833–2855.

Swart, N. C., and J. C. Fyfe (2012), Observed and simulated changes in the Southern Hemisphere surface westerly wind-stress, *Geophys. Res. Lett.*, *39*(L16711), doi:10.1029/2012gl052810.

Watts, D. R., C. Sun, and S. Rintoul (2001), A two-dimensional gravest empirical mode determined from hydrographic observations in the Subantarctic Front, *J. Phys. Oceanogr.*, *31*, 2186–2209.

Wijffels, S., D. Roemmich, D. Monselesan, J. Church, and J. Gilson (2016), Ocean temperatures chronicle the ongoing warming of Earth, *Nat. Clim. Change*, *6*, 116–118, doi:10.1038/nclimate2924.

Table 1. Cruises, years, and months for complete occupations of the SR1b section, with the batch(es) of standard seawater used for bottle salinity analysis for CTD calibration for SR1b stations on each cruise

| cruise | year/month | batch |
|---------|------------|---|
| JR00a | 1993/11 | p120 |
| JR00b | 1994/11 | p120 |
| JR16 | 1996/11 | unknown |
| JR27 | 1998/01 | p132 |
| JR47 | 2000/02 | p132 |
| JR55 | 2000/11 | p136 |
| JR67 | 2001/11 | p140 |
| JR81 | 2002/12 | p140 |
| JR94 | 2003/12 | p143 |
| JR115 | 2004/12 | p144 |
| JR139 | 2005/12 | p144 |
| JR163 | 2006/12 | p146 |
| JR193 | 2007/12 | p147 |
| JR194 | 2008/12 | p148 (stations 1-12), p149 (stations 13-32) |
| JC031 | 2009/02 | p150 |
| JR195 | 2009/11 | p150 |
| JR265 | 2011/12 | p151 |
| JR281 | 2013/03 | p154 (stations 2-14, 18, 20-28), p155 (stations 1, 15-17, 19, 29-31) |
| JR299 | 2014/03 | p155 |
| JR306 | 2015/01 | p156 |
| JR15003 | 2016/01 | p156 (stations 1-14), p158 (stations 15-31) |

Table 2. Trends, with 95% confidence intervals (see text), and standard deviations of conservative temperature Θ and its isopycnal property change (isopycnal) and isopycnal heave-driven (heave) components, averaged deeper than 2000 dbar over the whole section (all), or south (S) or north (N) of 58°S; and trends, with 95% confidence intervals, in scaled D_0 , D_s , and D_n (see Section 4)

| | trend (m°C yr ⁻¹) | standard deviation (°C) |
|----------------------|----------------------------------|----------------------------|
| all | | |
| Θ | -2.3±5.1 | 0.08 |
| isopycnal | -1.4±0.6 | 0.01 |
| heave | -1.4±4.8 | 0.07 |
| isopycnal + heave | -2.8±4.8 | 0.07 |
| D_0 | -2.9±4.3 | |
| S | | |
| Θ | 0.1±4.0 | 0.06 |
| isopycnal | -2.2±0.9 | 0.02 |
| heave | 1.8±3.3 | 0.05 |
| isopycnal + heave | -0.4±3.8 | 0.06 |
| D_s | 0.3±3.5 | |
| N | | |
| Θ | -4.5±8.1 | 0.12 |
| isopycnal | -0.8±0.5 | 0.01 |
| heave | -4.1±7.8 | 0.12 |
| isopycnal + heave | -4.9±7.6 | 0.12 |
| D_n | -5.6±7.3 | |

Figure 1. (a): Nominal SR1b hydrographic stations (squares) and line, with climatological locations (gray) of the Subantarctic Front (SAF), Polar Front (PF), and Southern ACC Front (SACCF) [Orsi *et al.*, 1995] and bathymetry (color contours, [Arndt *et al.*, 2013; Smith and Sandwell, 1997]). (b): Latitude-depth section of SR1b mean conservative temperature $\bar{\Theta}$ (filled color contours) and mean neutral density $\bar{\gamma}_n$ (dark gray contours), with indicative front locations based on the SR1b time-mean temperature and salinity sections marked at top along with the Antarctic Zone (AZ) and Polar Frontal Zone (PFZ). (c): Time series of Θ averaged over the area deeper than 2000 dbar (blue solid line and circles), with the linear trend (dashed line). The white shading near the bottom in (b) marks the area where the isopycnal/heave decomposition does not produce values at certain times (see Section 3); these areas are not included in the spatially-averaged time series.

Figure 2. (a) Time series of the deviation (relative to the time mean, $\bar{\Theta}$) in section-averaged Θ deeper than 2000 dbar (dark blue, circles) and its isopycnal (dark green, squares) and heave (magenta, triangles) components, with the trends in each component shown by dashed lines. The reconstructed (isopycnal + heave) total is shown by the thick gray line. (b) Time series of the isopycnal component of Θ deeper than 2000 dbar averaged across the section (dark green, as in (a)), south of 58°S (cyan), and north of 58°S (orange), with trends as dashed lines.

Figure 3. Standard deviations of time series of (a) Θ and its (b) isopycnal and (c) heave components, with mean γ_n contours in dark gray as marked in (a). The color scale is nonlinear.

Figure 4. Trends in (a) conservative temperature Θ and in its (c) isopycnal and (e) heave components, with mean γ_n contoured in dark gray (at levels marked in (a)). The color scale is nonlinear. On (e) the γ_n trend over 20 years is indicated by movement from light gray to black contours. Trends in average temperature or component at each depth south (cyan) and north (orange) of 58°S are plotted in (b), (d), and (f), with dotted lines indicating 95% confidence intervals (in (b) and (f) the lower bounds of the confidence intervals for the northern region fall outside the horizontal axis limits of the plot). In (b) the dashed lines are the sum of the components shown in (d) and (f), while the solid lines are the original total temperature trend. Trends in (a), (c), and (e) are shown for all grid points where Equation 3 produces values in at least 50% of occupations, with the white shading (as in Figure 1b) marking points where it is not defined in the initial and/or final occupations; these areas are not included in spatial averages (e.g. (b), (d), and (f)).

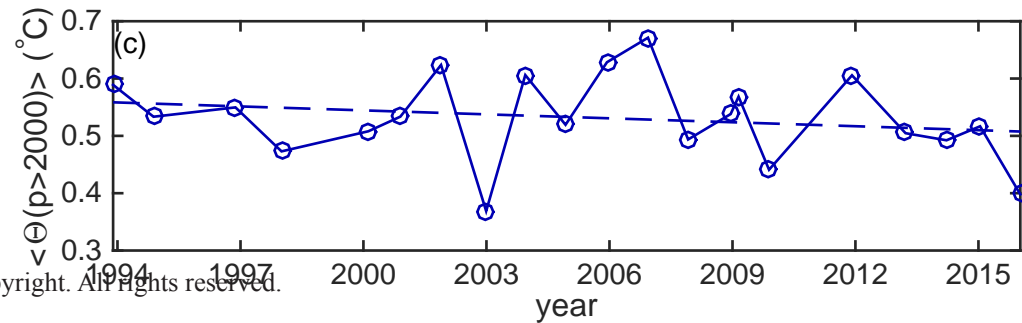
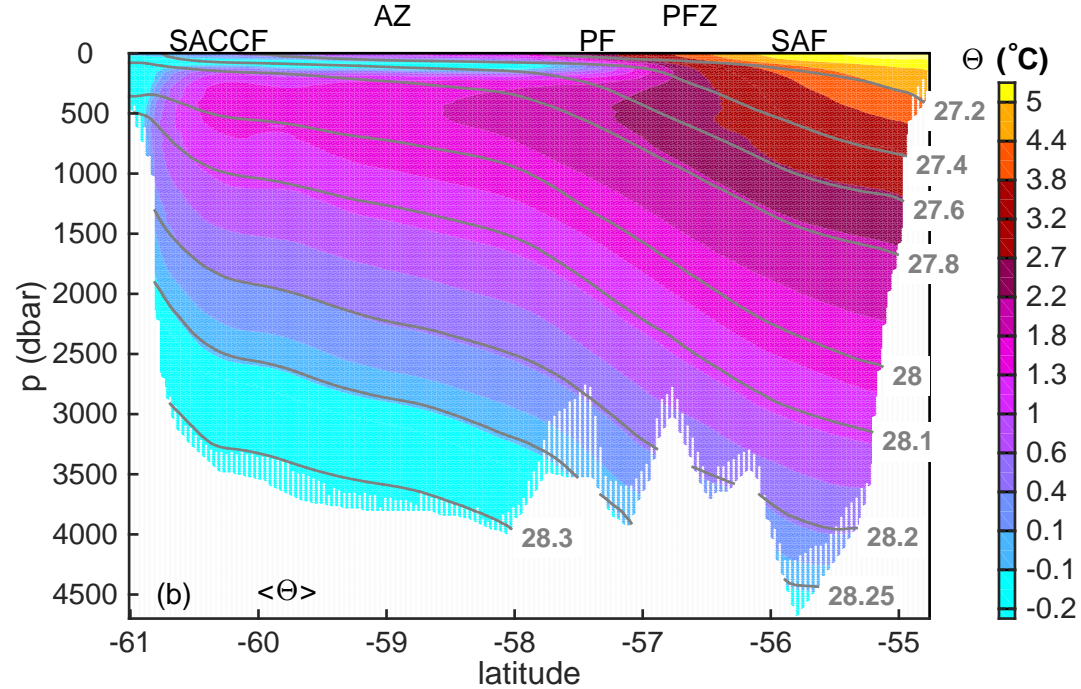
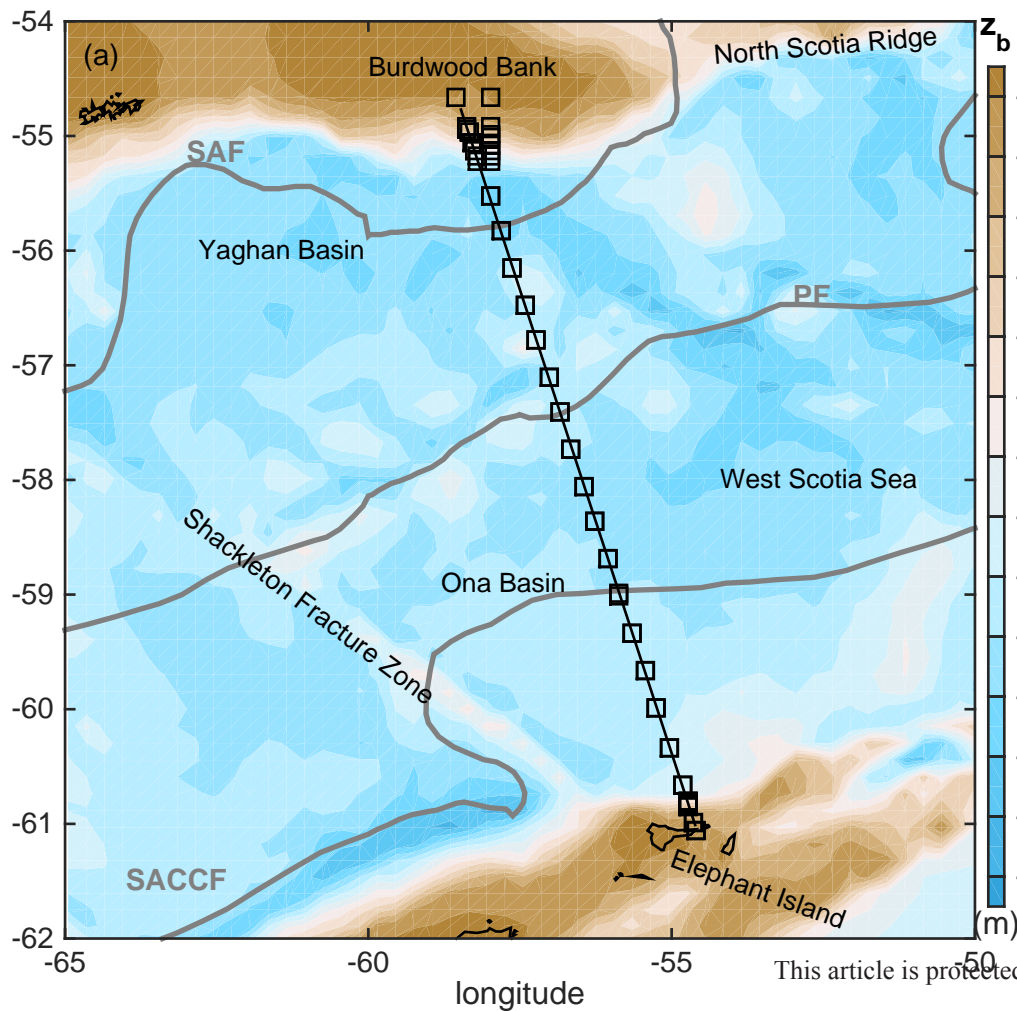
Figure 5. Conservative temperature Θ plotted against absolute salinity S_A from the 21 occupations of SR1b, at a range of pressure levels deeper than 1000 dbar (colors, as marked on plot) and latitudes (circle sizes, as marked on plot), for the 21 occupations, with neutral density γ_n contours at 2000 dbar (dark gray, as marked, with pale gray at intervening 0.1 kg m^{-3} intervals).

Figure 6. Correlations between Θ and frontal position proxy D . (a) Θ deeper than 2000 dbar averaged across the section, plotted against integrated frontal position proxy D_0 (dark blue); Θ south of 58°S (Θ_S), plotted against southern frontal position proxy D_S (cyan); Θ north of 58°S (Θ_N), plotted against northern frontal position proxy D_n (orange), with best-fit lines as labeled. Correlations between (b) $\Theta(y, p, t)$ and $D_0(t)$; (c) $\Theta(y, p, t)$ and $D_S(t)$; and (d) $\Theta(y, p, t)$ and $D_n(t)$. Cyan lines in (c) and orange lines in (d) mark the limits of integration for D_S and D_n , respectively. (e) Profiles of correlations for conservative temperature averaged along pressure surfaces: correlations between $\Theta(y, t)$ and $D_0(t)$ (dark blue); $\Theta_S(y, t)$ and $D_S(t)$ (cyan); and $\Theta_N(y, t)$ and $D_n(t)$ (orange).

Figure 7. (a) Time series of Θ deeper than 2000 dbar (dark blue: section-averaged $\langle\Theta\rangle$, cyan: $\langle\Theta\rangle_S$, orange: $\langle\Theta\rangle_N$), with frontal position proxies D_0 , D_S , and D_n (dark purple, triangles) scaled and offset to best fit $\langle\Theta\rangle$, $\langle\Theta\rangle_S$, and $\langle\Theta\rangle_N$, respectively (with coefficients indicated by on-panel text). Time series of altimeter frontal position proxy D^{ssh} , with the same scale factors and offsets applied, are shown in pale purple, with values interpolated to SR1b section times marked by triangles connected by thick light purple lines. (b) Residuals: $\Theta - (0.7 + 1.6D_0)$ (dark blue), $\Theta_S - (-0.1 + 5.1D_S)$ (cyan), and $\Theta_N - (1.3 + 2.9D_n)$ (orange).

Accepted Article

Figure 1.



Accepted Article

Figure 2.

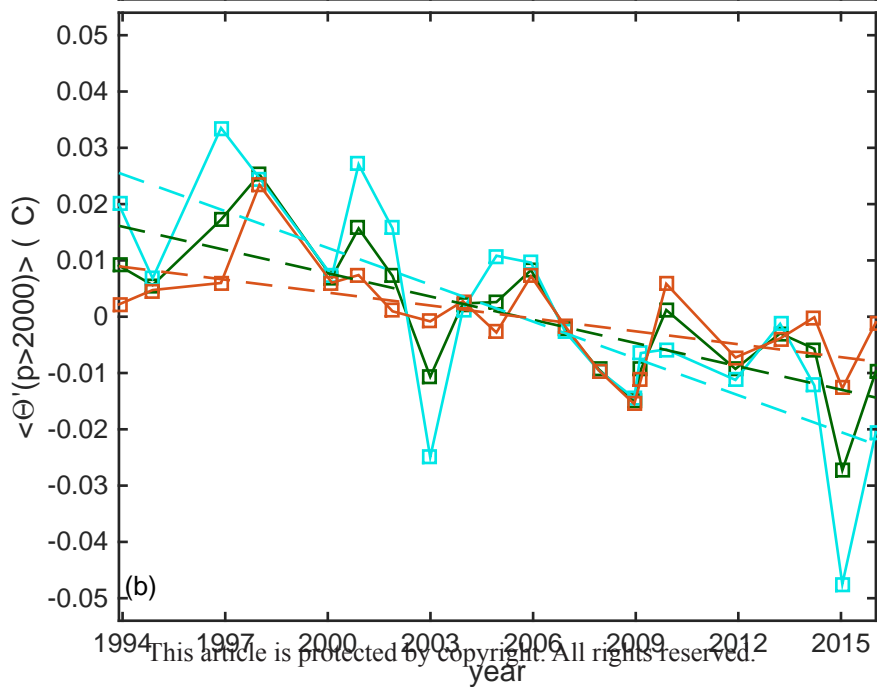
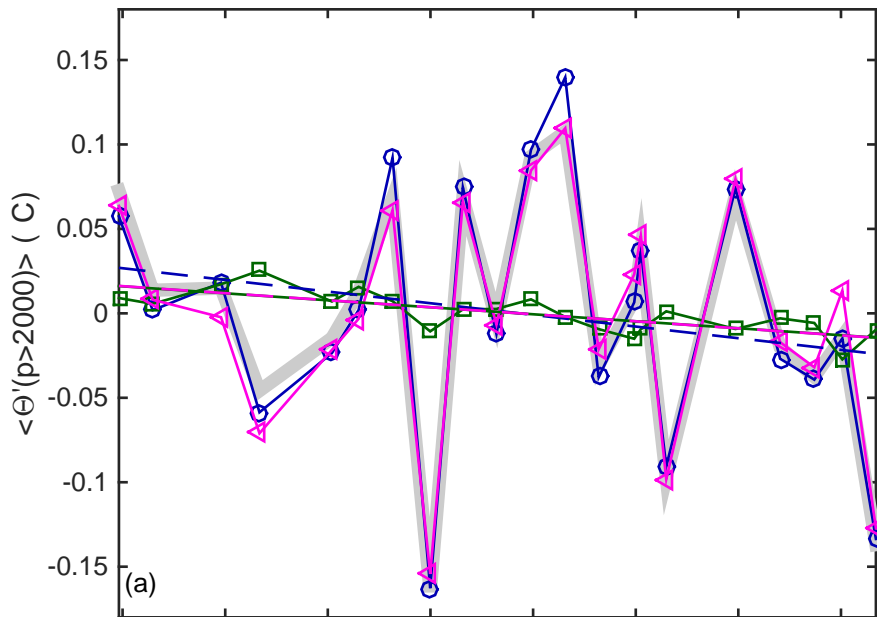


Figure 3.

Accepted Article

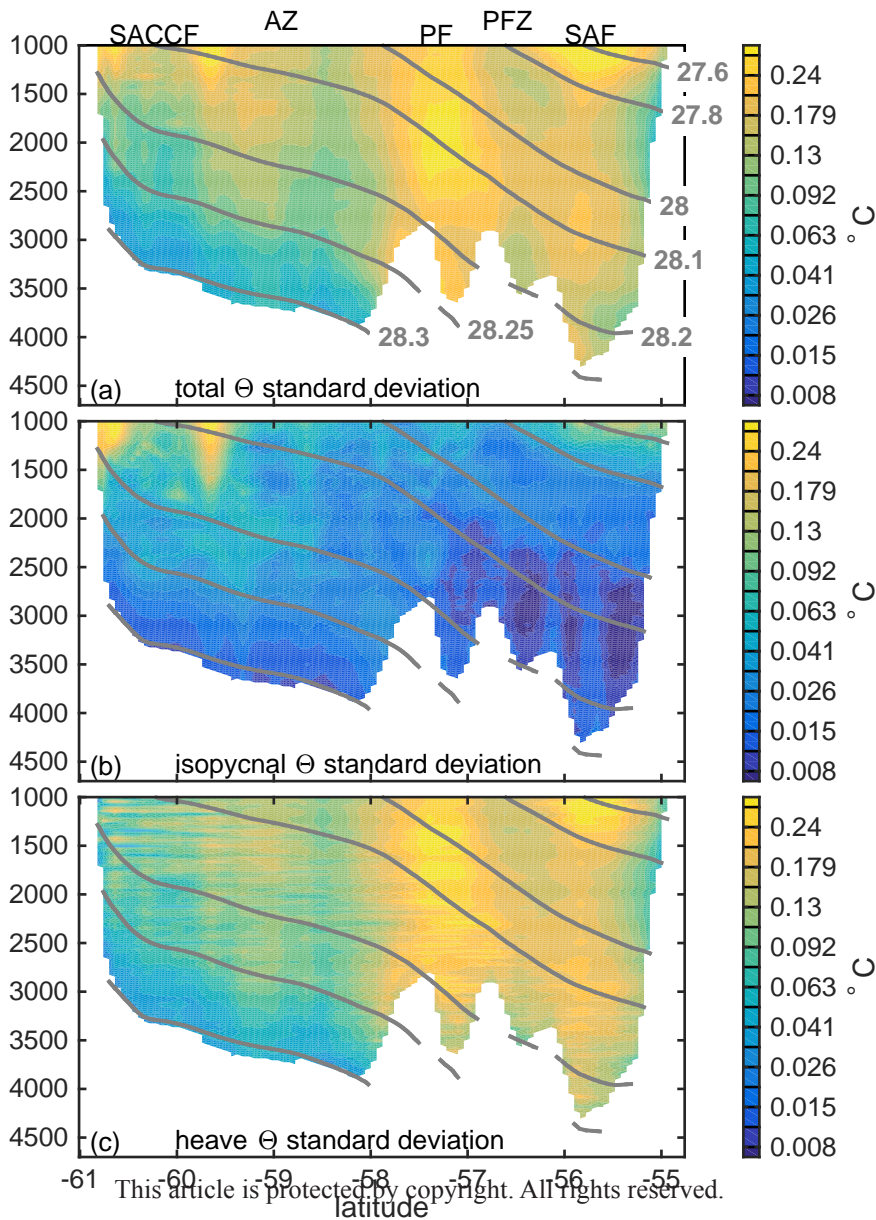
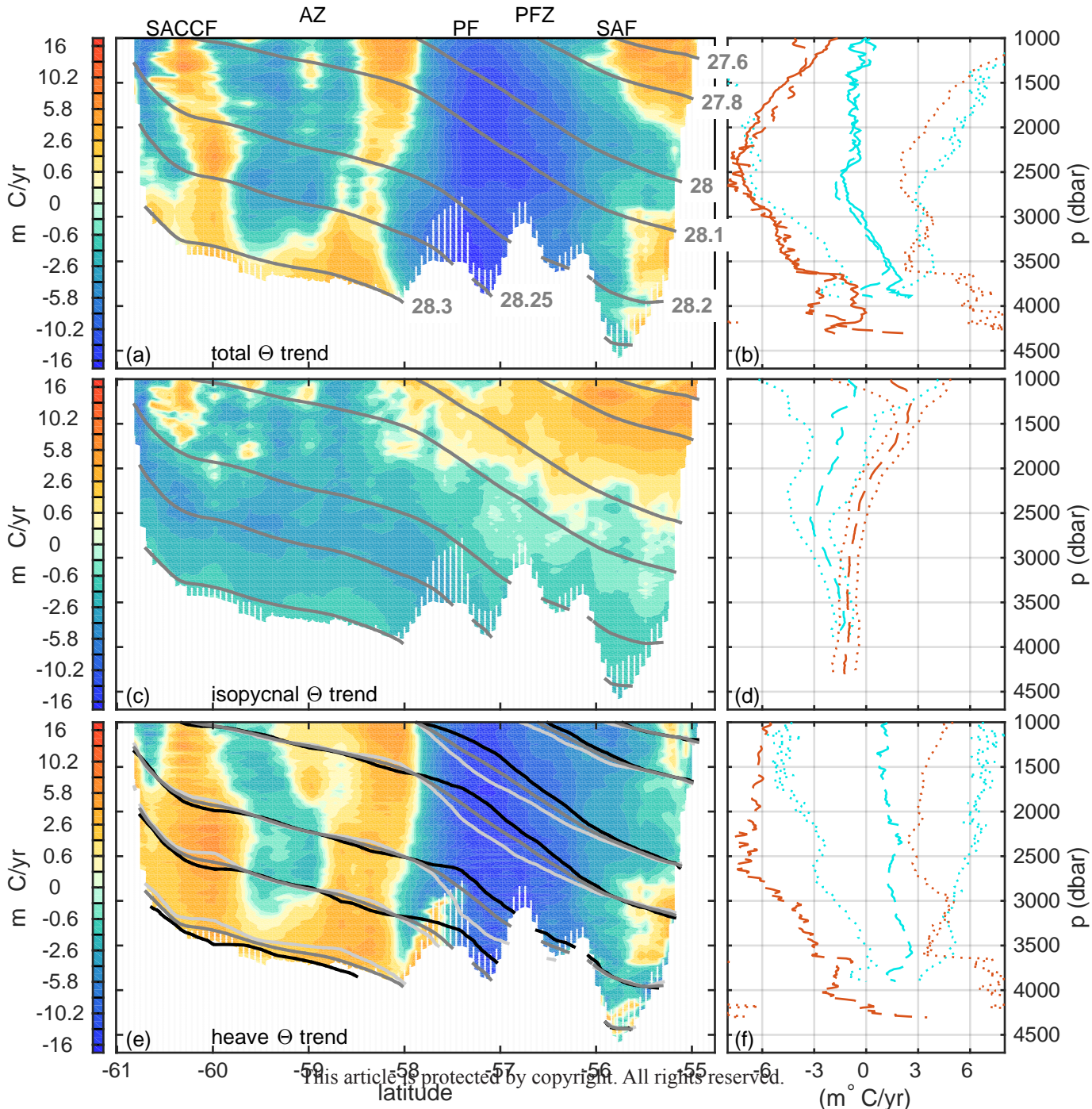


Figure 4.

Accepted Article



Accepted Article

Figure 5.

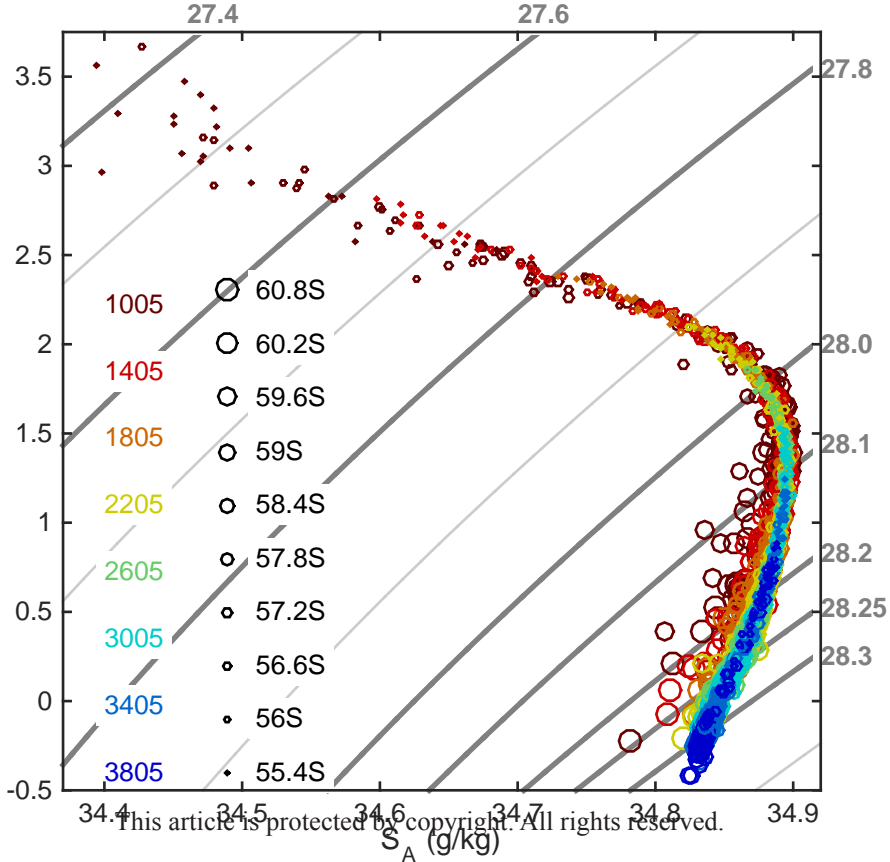


Figure 6.

Accepted Article

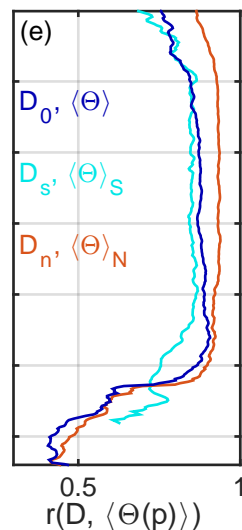
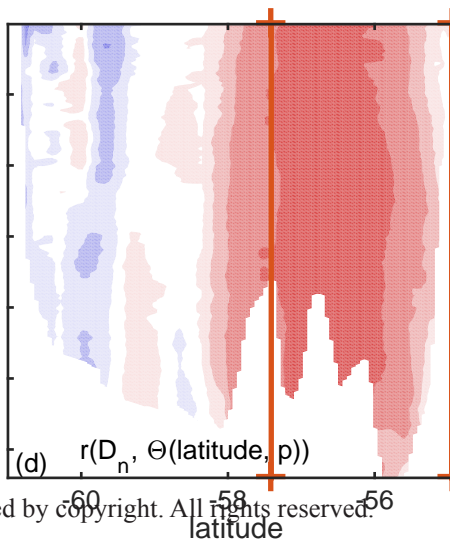
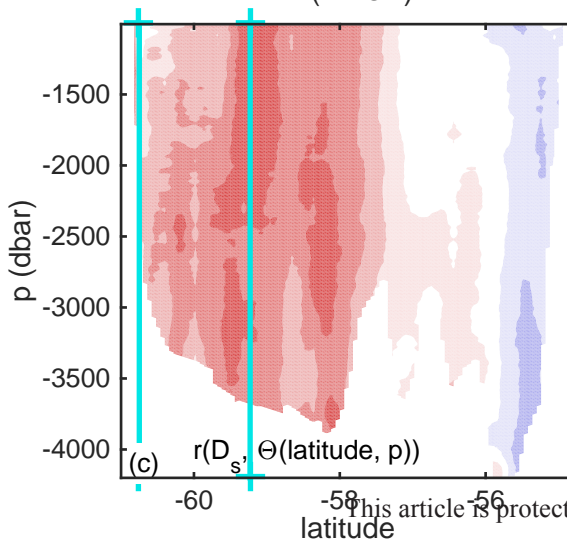
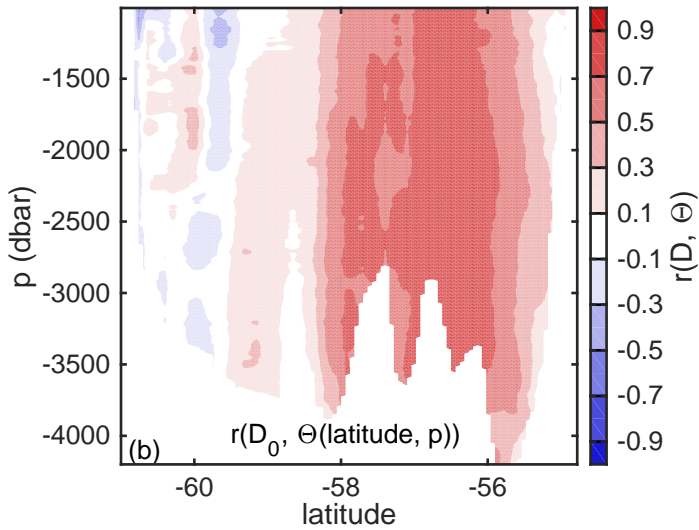
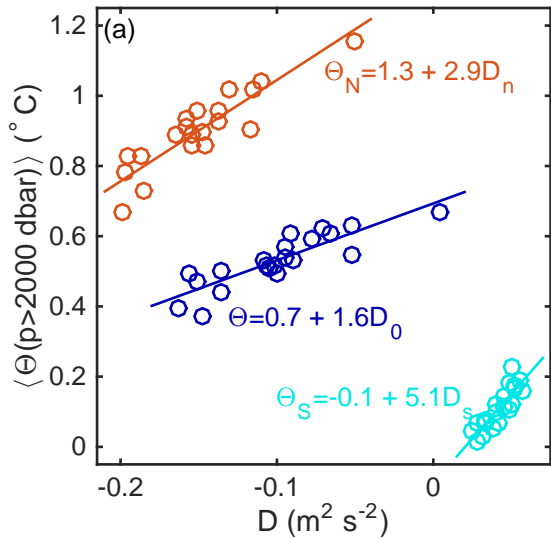


Figure 7.

Accepted Article

